

Supporting Information

Laser synthesis of clean mesocrystal of cupric oxide for efficient gas sensing

Zhe Li,^a Cun-Ku Dong,^a Jing Yang,^a Shi-Zhang Qiao,^b Xi-Wen Du^{a,*}

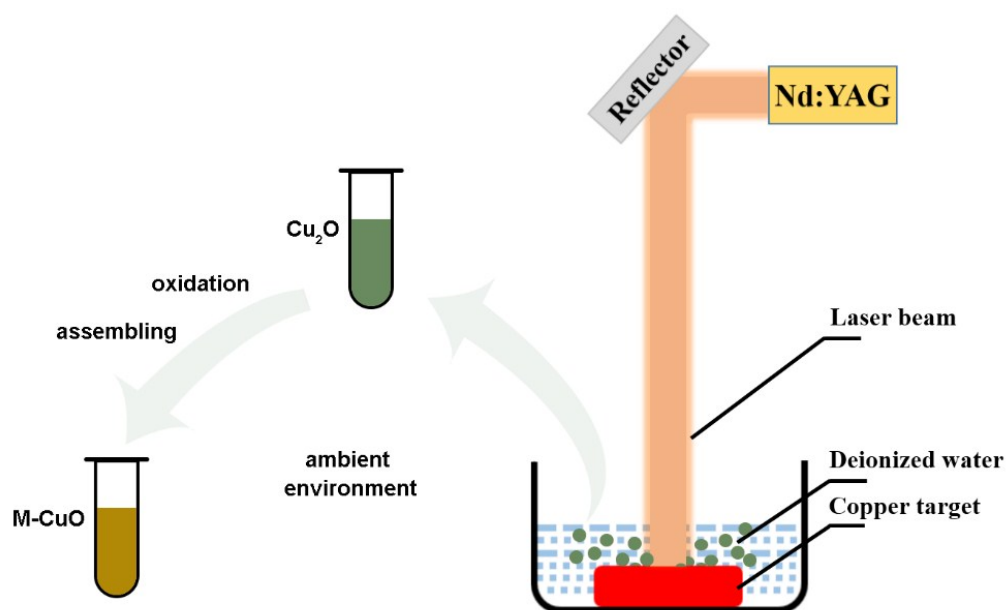
^a *School of Materials Science and Engineering, Tianjin University, Tianjin 300072, China*

^b *School of Chemical Engineering, The University of Adelaide, SA 5005, Australia*

*Email: xwdu@tju.edu.cn

1. Materials.

Sodium hydroxide (NaOH) and $\text{NH}_3 \cdot \text{H}_2\text{O}$ (25-28% wt.%) were purchased from Komiou Chemical Reagent Co., LTD. Cupric nitrate ($\text{Cu}(\text{NO}_3)_2$) was purchased from Sinopharm Chemical Reagent Co., LTD. Cupric acetate ($\text{Cu}(\text{Ac})_2$) was purchased from Fengchuan Chemical Reagent Technologies Co., LTD. Hydrochloric acid (38% wt.) were purchased from Jiangtian chemical technology Co., LTD. Copper target (purity quotient $\geq 99.99\%$) was purchased from Incole Union Technology Co., LTD. All the reagents are of analytical grade and are used without further purification.



Scheme S1 Schematic illustration on the synthesis of M-CuO.

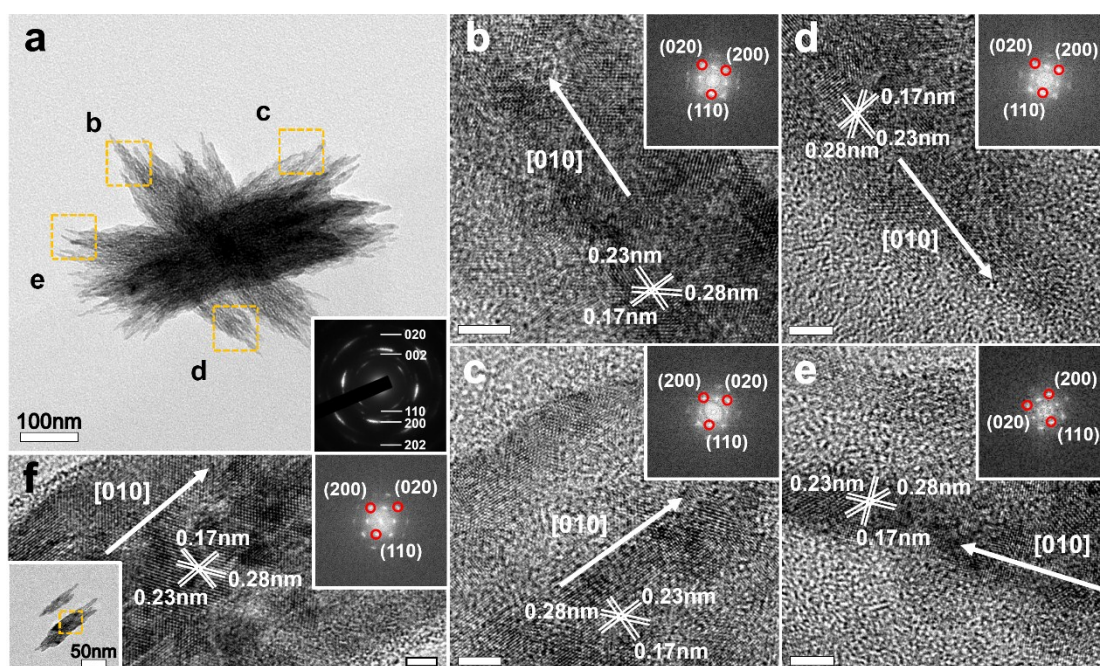


Fig. S1 TEM and HRTEM images of M-CuO bundles. (a) TEM image. (b)-(e) HRTEM images of the selected areas in (a), the insets are the corresponding FFT patterns. (f) HRTEM image of a single M-CuO spindle. The top and bottom insets are the FFT pattern and low magnification TEM image, respectively. The scale bars in (b)-(f) represent 5 nm.

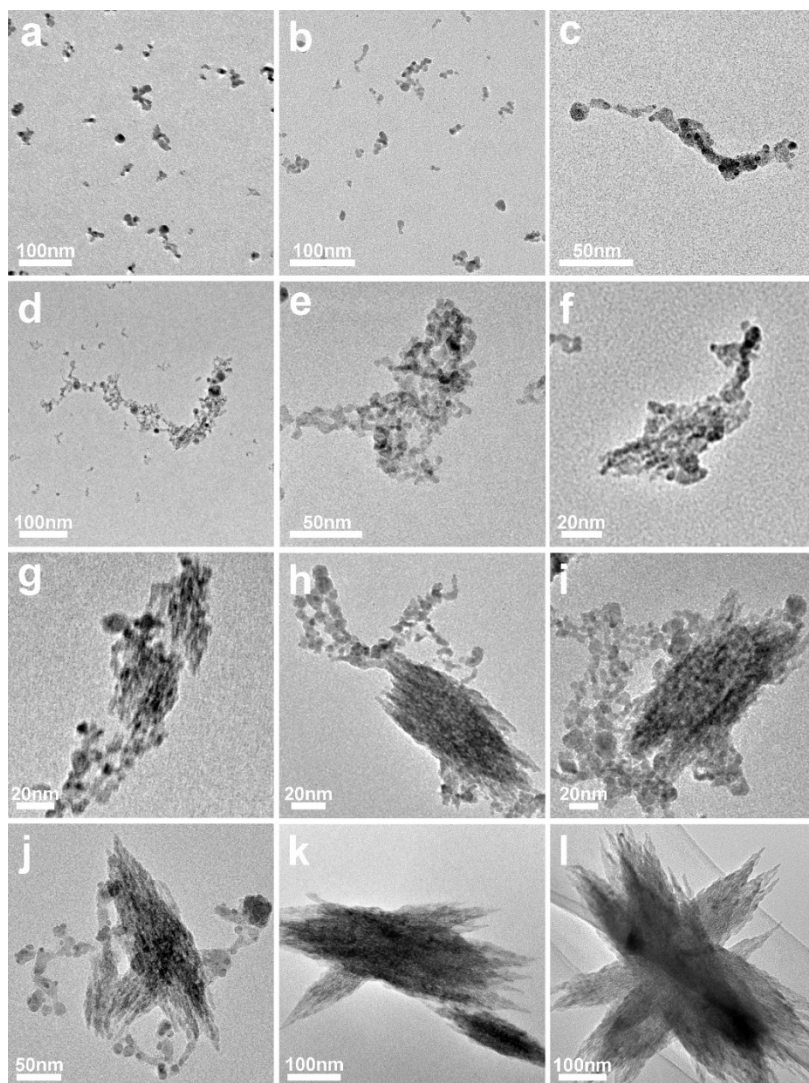


Fig. S2 TEM observation on morphological evolution of M-CuO. (a) Cu_2O nanoparticles. (b) CuO nanoparticles transformed from Cu_2O nanoparticles. (c)-(e) connection of individual CuO nanoparticles into a loose agglomerate. (f), (g) a cylinder CuO formed by growing along [010] direction. (h)-(j) CuO spindle formed via epitaxial growth mainly along [010] and [100]. (k), (l) A CuO bundle composed of CuO spindles.

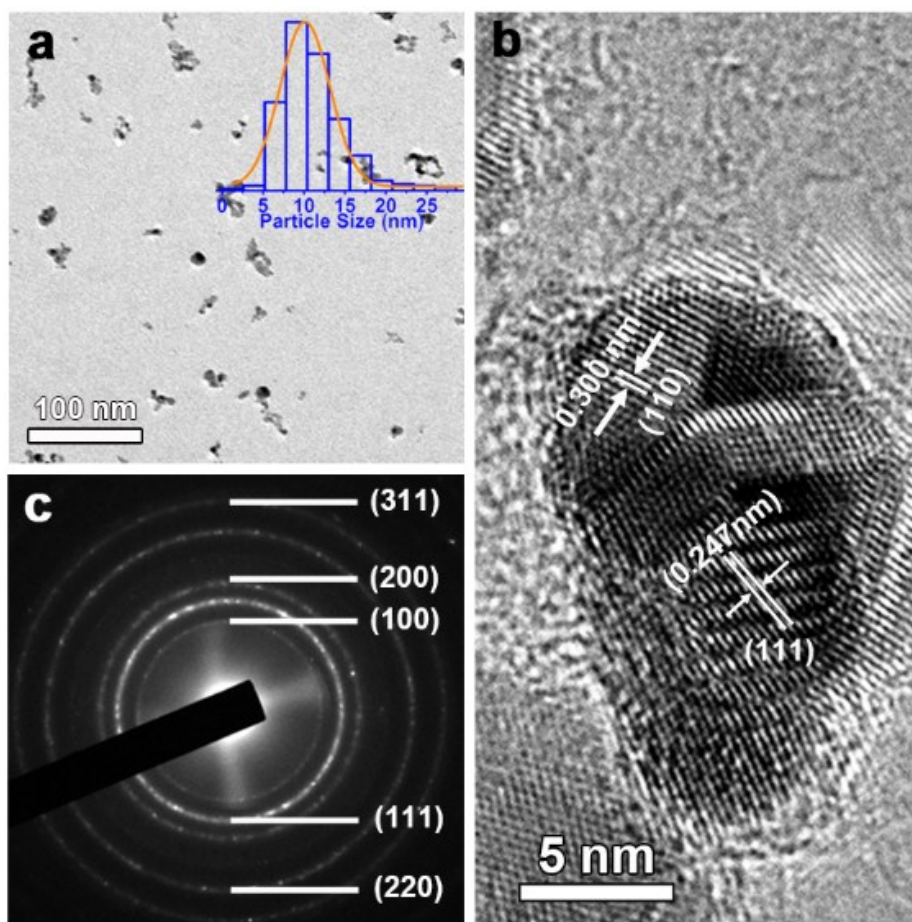


Fig. S3 Characterization of Cu₂O nanoparticles. (a) TEM image, the inset is size distribution, (b) HRTEM image, and (c) SAED pattern.

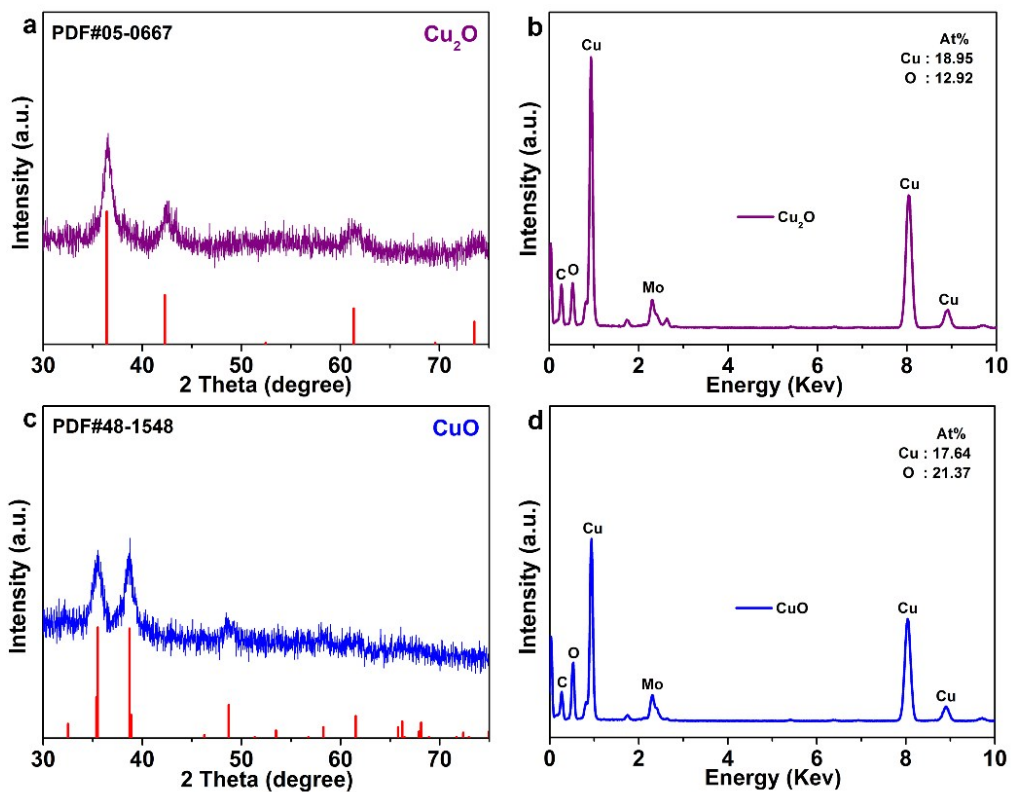


Fig. S4 Phase structure and composition of Cu_2O and CuO nanoparticles. (a), (b) XRD and EDS profiles of as-prepared Cu_2O nanoparticles. (c), (d) XRD and EDS profiles of CuO nanoparticles after the oxidization in air.

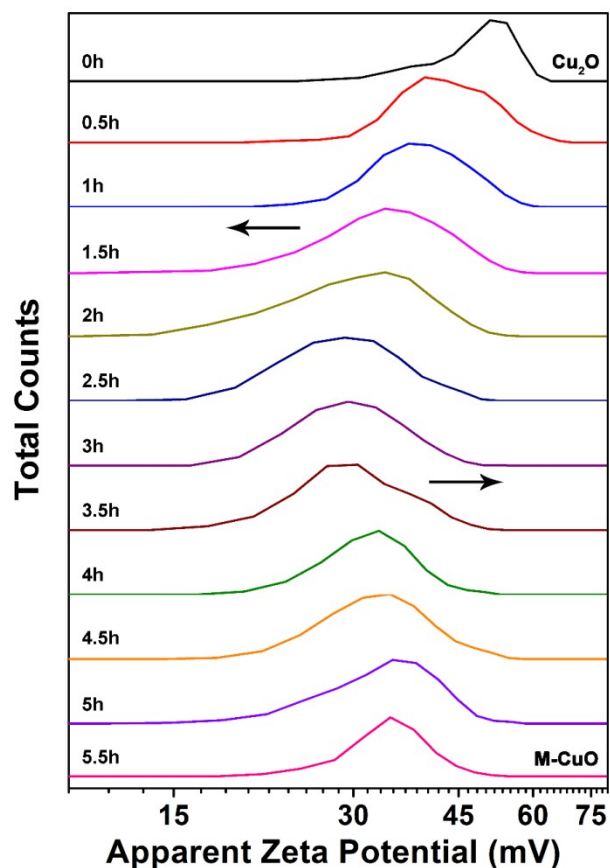


Fig. S5 The zeta potential change of product obtained via PLAL technique over time. The zeta potential of every moment: 0 h-48.9 mV, 0.5 h-44.4 mV, 1 h-40.3 mV, 1.5 h-36 mV, 2 h-32.5 mV, 2.5 h-30.6 mV, 3 h-27.3 mV, 3.5 h-31.4 mV, 4 h-32.9mV, 4.5 h-34.4 mV, 5 h-35.1 mV, 5.5 h-35.2 mV. The top arrows marks the decrease of zeta potential from Cu_2O nanoparticles to CuO nanoparticles in the process of oxidation, and the bottom arrows illustrates the increase of zeta potential from CuO nanoparticles to final M-CuO in the process of self-assembling.

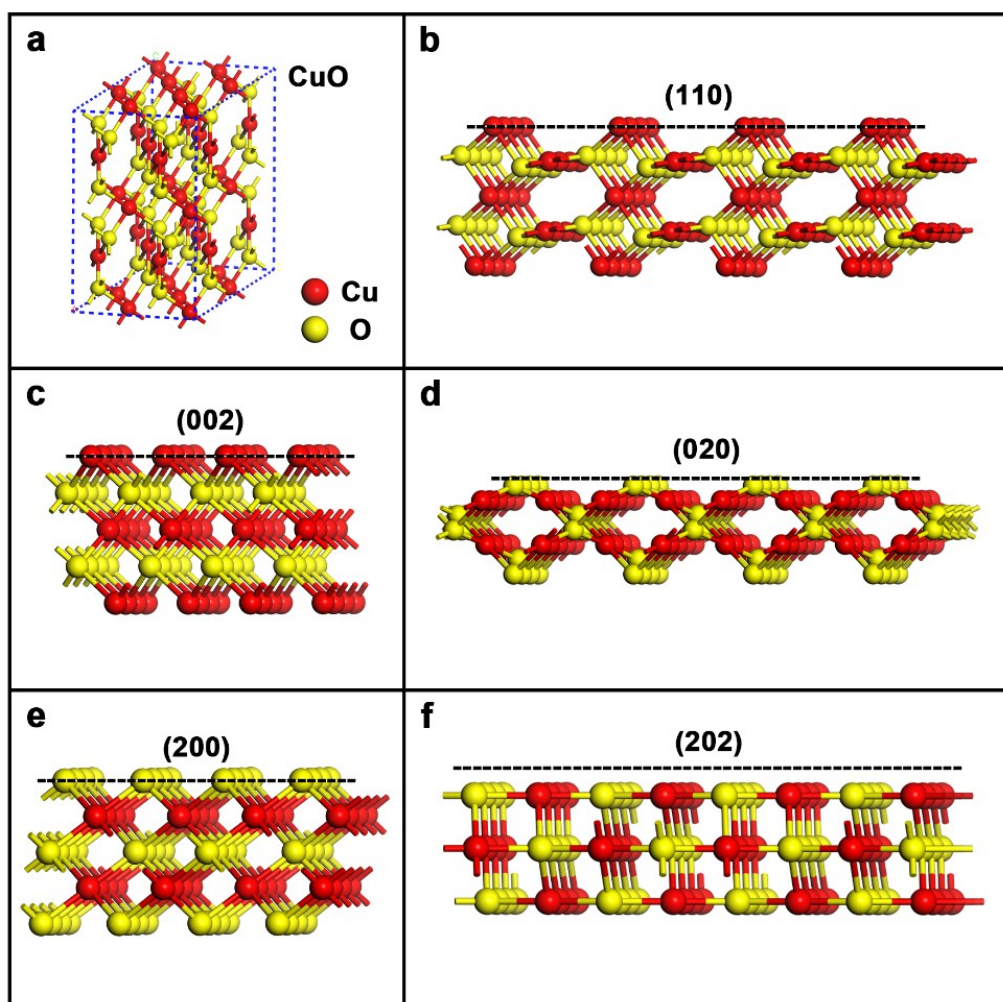


Fig. S6 Crystal model of M-CuO. (a) a monoclinic CuO unit cell. (b) (110) plane and (c) (002) plane, both of which are terminated by copper atoms. (d) (020) plane and (e) (200) plane, both of are terminated by oxygen atoms. (f) (202) plane terminated by interlaced copper atoms and oxygen atoms.

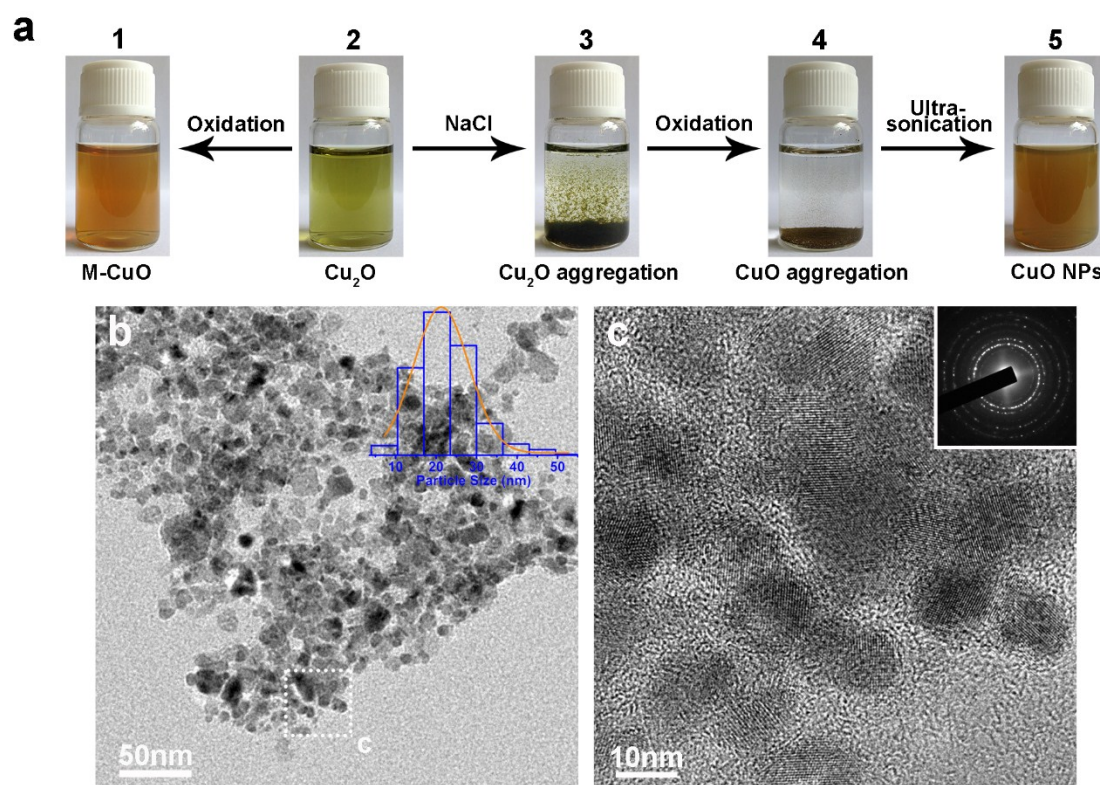


Fig. S7 Characterizations of CuO products deriving from different formation processes. (a) Photographs on appearance change. (a1) M-CuO by direct oxidation and assembling of Cu₂O nanoparticles, (a2) Cu₂O precursor, (a3) aggregation of Cu₂O nanoparticles immediately after NaCl was added, (a4) CuO agglomerate after 5 hour oxidation, (a5) CuO nanoparticles by ultrasonic treatment of CuO agglomerate. (b) TEM image of CuO nanoparticles in a5, the insert is the diagram of size distribution, (c) HRTEM image, and the inset is a SAED pattern.

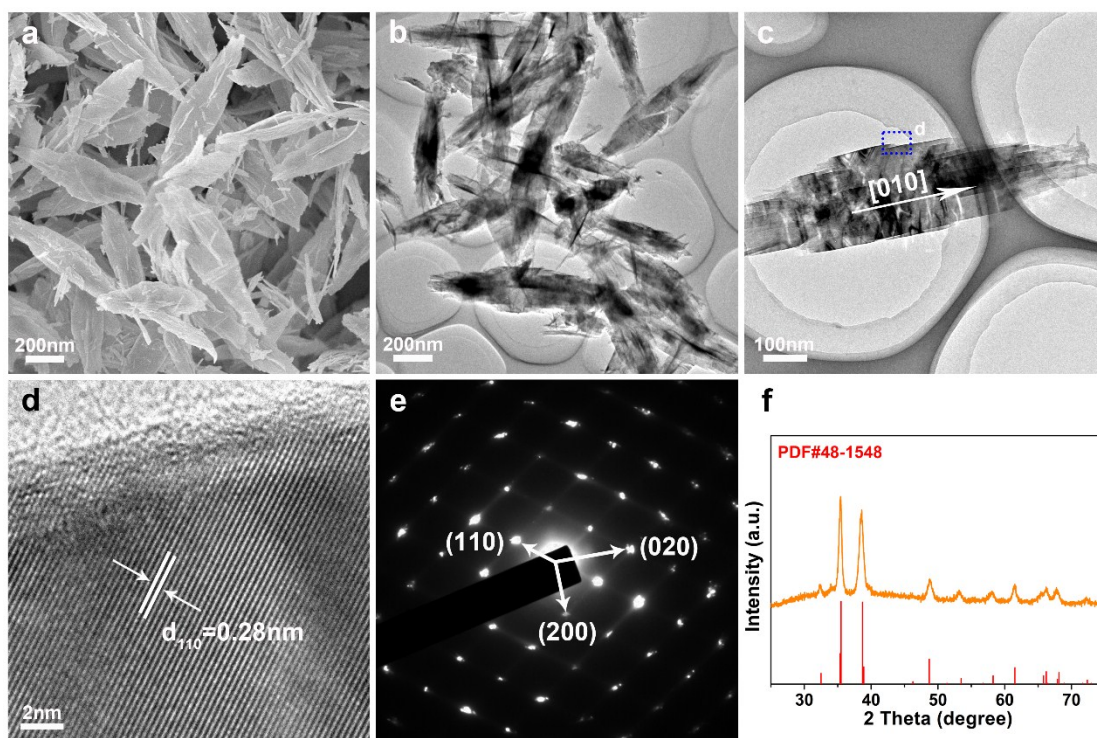


Fig. S8 Characterizations of S-CuO. (a) SEM image. (b), (c) TEM images of at different magnifications. (d) HRTEM image of selected area in (c). (e) SAED pattern. (f) XRD pattern.

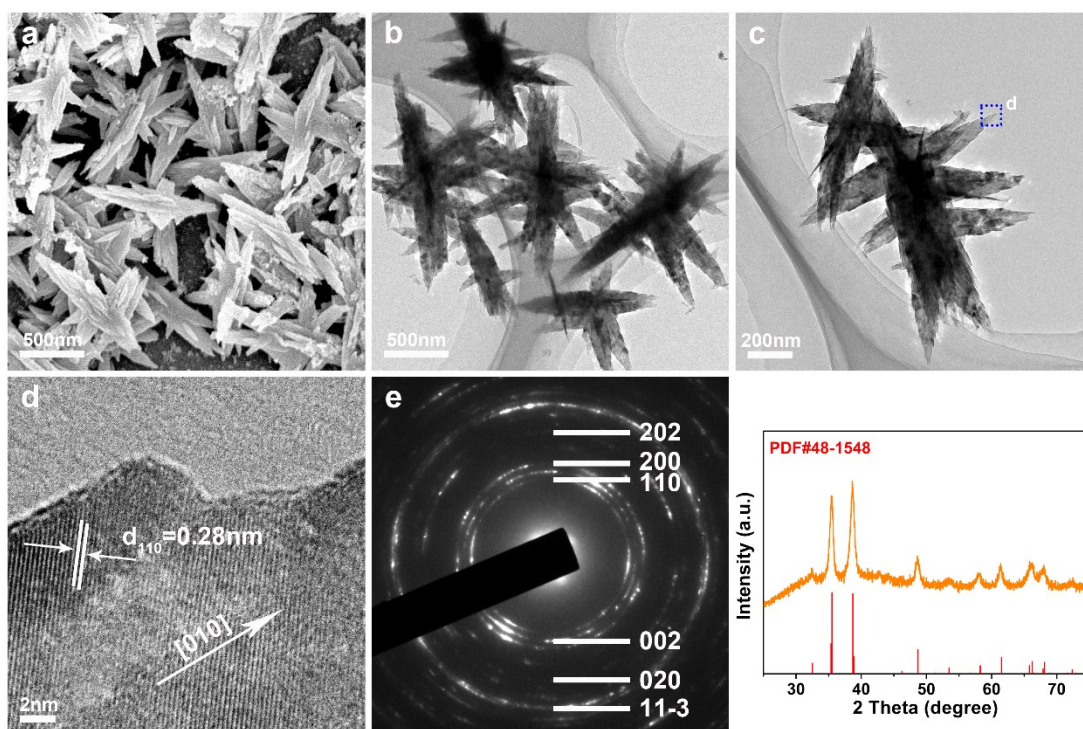


Fig. S9 Characterizations of P-CuO. (b), (c) TEM images of at different magnifications. (d)

HRTEM image of selected area in (c). (e) SAED pattern. (f) XRD pattern.

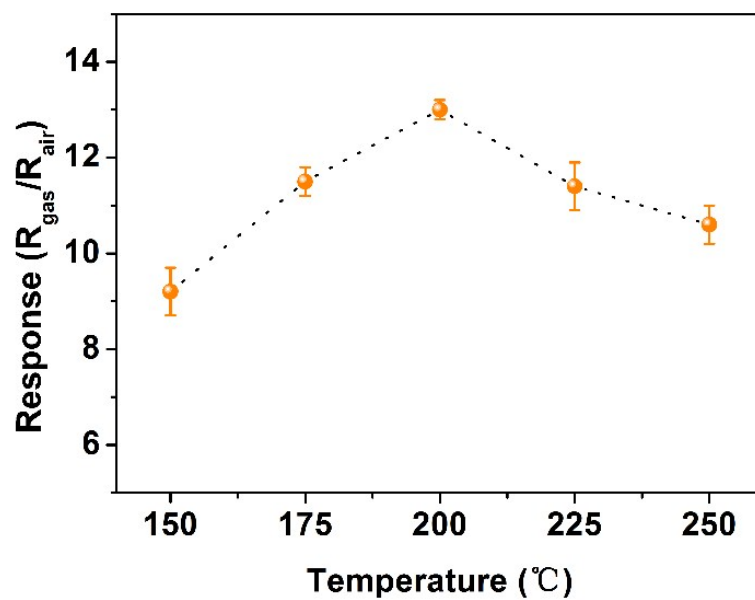


Fig. S10 The optimum working temperature of M-CuO under 200ppm of gaseous ethanol.

Table S1. Summary on gas sensing performance of CuO materials

Materials	Gas concentration (ppm)	Response (R _g /R _a)	Refs
M-CuO	200	13	This work
	100	7.3	
	50	4.2	
	25	2.7	
CuO nanosheets	200	2.5	[1]
	20	1.5	
CuO microspheres	200	2.3	[2]
	100	1.9	
	50	1.6	
	20	1.3	
Commercial CuO powder	200	1.7	[2]
	100	1.5	
	50	1.4	
	20	1.2	
Ag-CuO heterojunction	200	5	[2]
	100	4	
	50	3.2	
	20	2.3	
CuO nanorods	200	6.5	[3]
	100	5	
	50	3.5	
	20	2	
CuO nanofilms	200	1.2	[4]
CuO/In ₂ O ₃ core-shell nanorods	200	7.3	[5]
	150	6.2	
	100	4.7	
	50	3.8	
Belt-like CuO	250	4.5	[6]
	100	3.6	
	50	3.1	
	20	2.5	
Willow-leaf-like nanoplates CuO	250	2.5	[6]
	100	2.1	
	50	1.9	
	20	1.7	
Quasi-square nanoplates CuO	250	4.7	[6]
	100	3.6	
	50	3	
	20	2.3	

	250	3.9	
Rod-like CuO	100	3.2	[6]
	50	2.7	
	20	2.2	

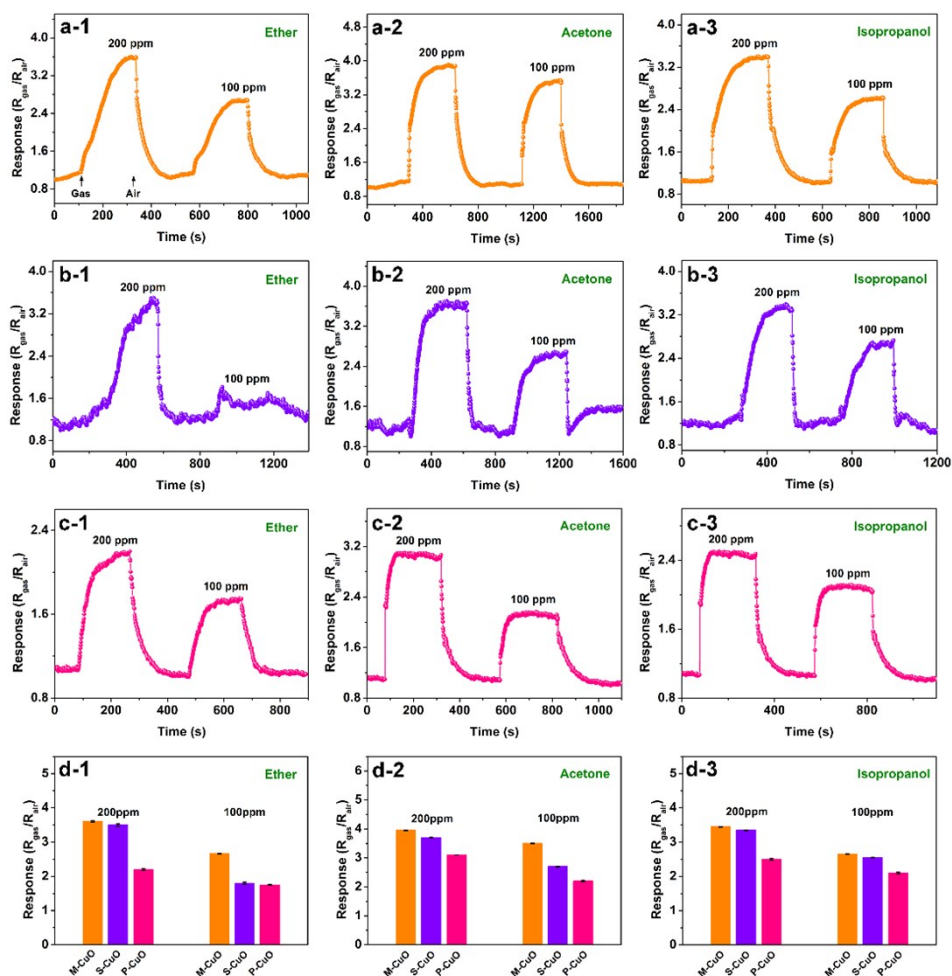


Fig. S11 Gas sensing properties of the gas sensors composed of M-CuO, S-CuO and P-CuO under 200 and 100 ppm of gaseous ether, acetone and isopropanol at operating temperature of 200 °C. (a1)-(a3) M-CuO for ether, acetone and isopropanol, respectively. (b1-b3) S-CuO for ether, acetone and isopropanol, respectively. (c1-c3) P-CuO for ether, acetone and isopropanol, respectively. (d1-d3) Comparison on the M-CuO, S-CuO and P-CuO for ether, acetone and isopropanol under 200 and 100 ppm, respectively.

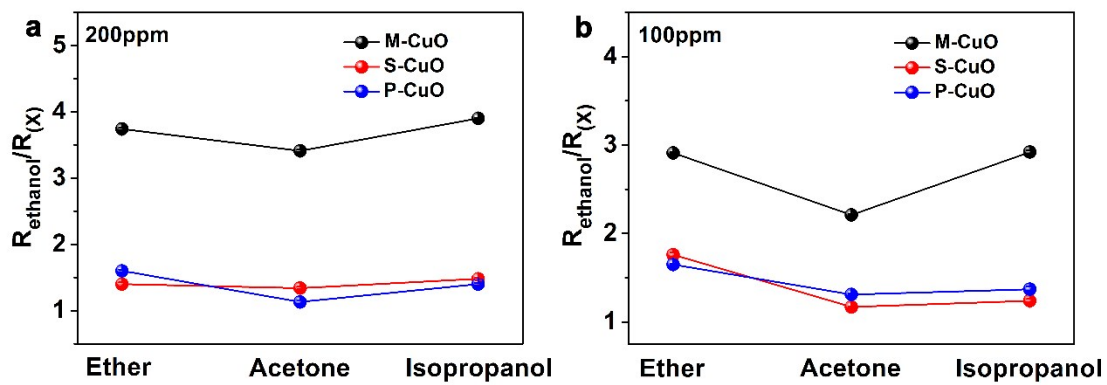


Fig. S12 The selectivity of M-CuO, S-CuO and P-CuO for ethanol at different concentrations.

(a) 200 ppm. (b) 100 ppm. The ordinate ($R_{\text{ethanol}}/R_{(x)}$) is the sensitivity ratio of ethanol to other gases (ether, acetone or isopropanol).

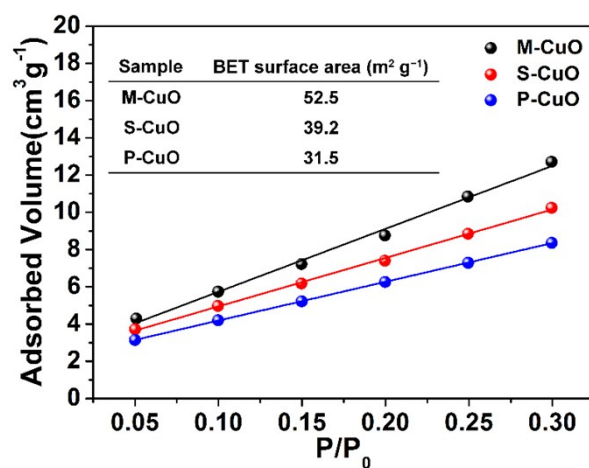


Fig. S13 Nitrogen adsorption–desorption isotherms (BET) linear fittings for M-CuO, S-CuO and P-CuO. Specific surface area of M-CuO, S-CuO and P-CuO is determined as 52.5, 39.2 and 31.5 m^2g^{-1} , respectively.

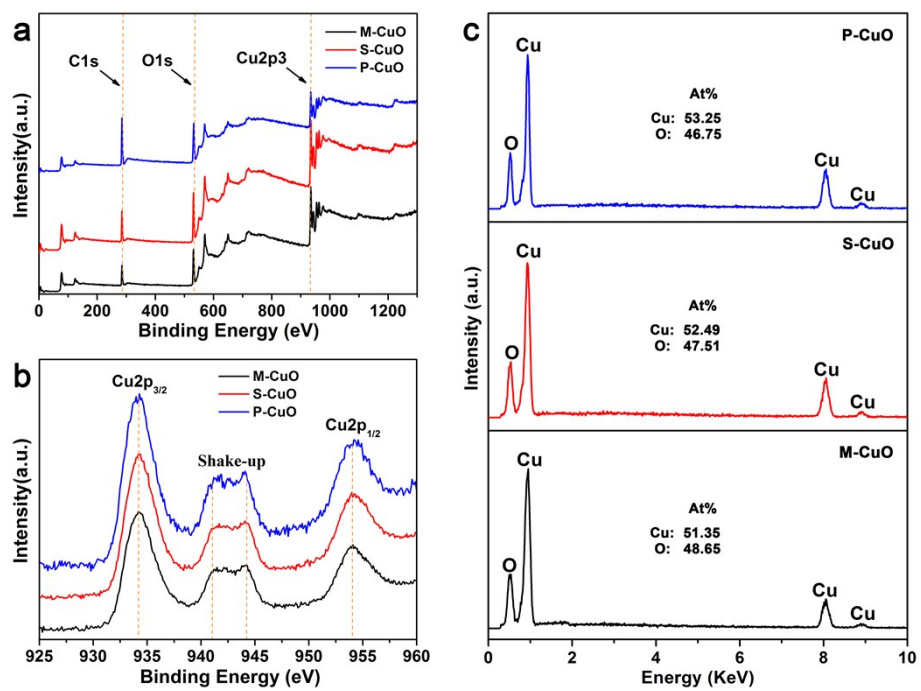


Fig. S14 XPS and EDS comparisons of M-CuO, S-CuO and P-CuO. (a) XPS survey spectra. (b) XPS core-level spectra of Cu2p. (c) EDS results.

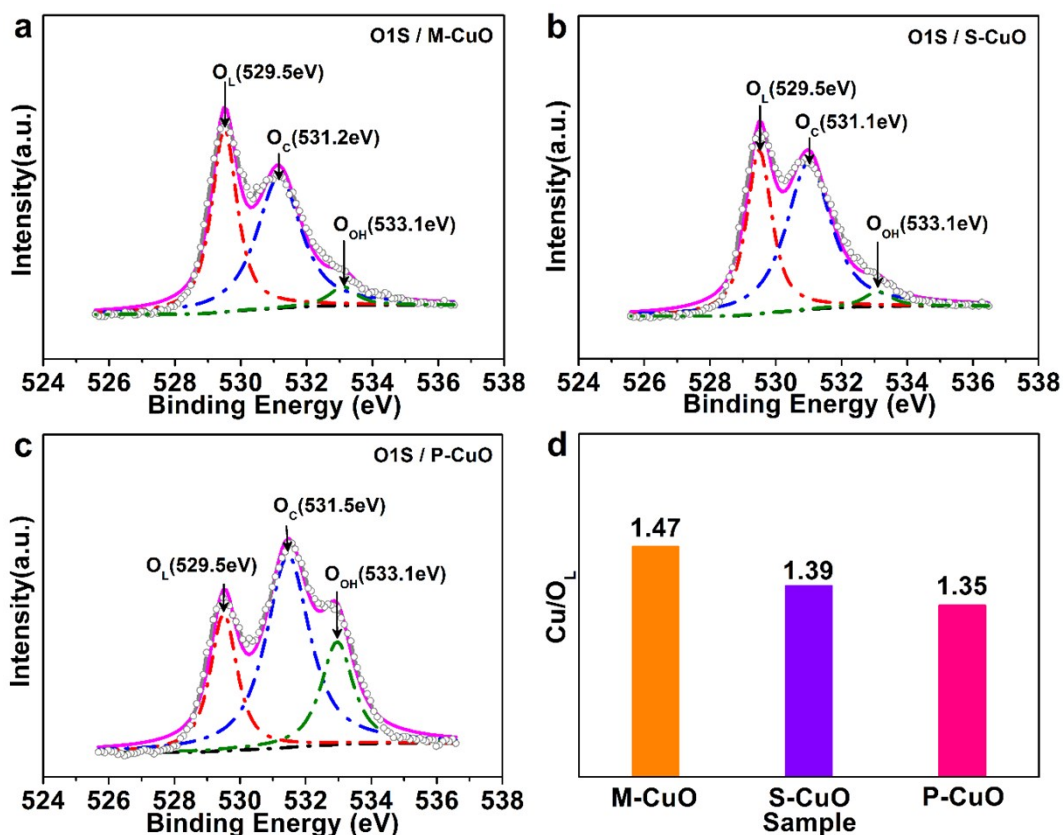


Fig. S15 XPS core-level spectra of O1s for three CuO structures. (a) M-CuO, (b) S-CuO, (c) P-CuO. The peak at 529.5 eV is attributed to the lattice oxygen (O_L) of CuO, and the peak at 531.1–531.6 eV is assigned to the chemisorbed oxygen species (O_C), whereas the peak at 533.1 eV arises from the oxygen in hydroxyl of physically adsorbed H_2O ^{7–11}. (d) Cu/O_L ratio of M-CuO, S-CuO and P-CuO.

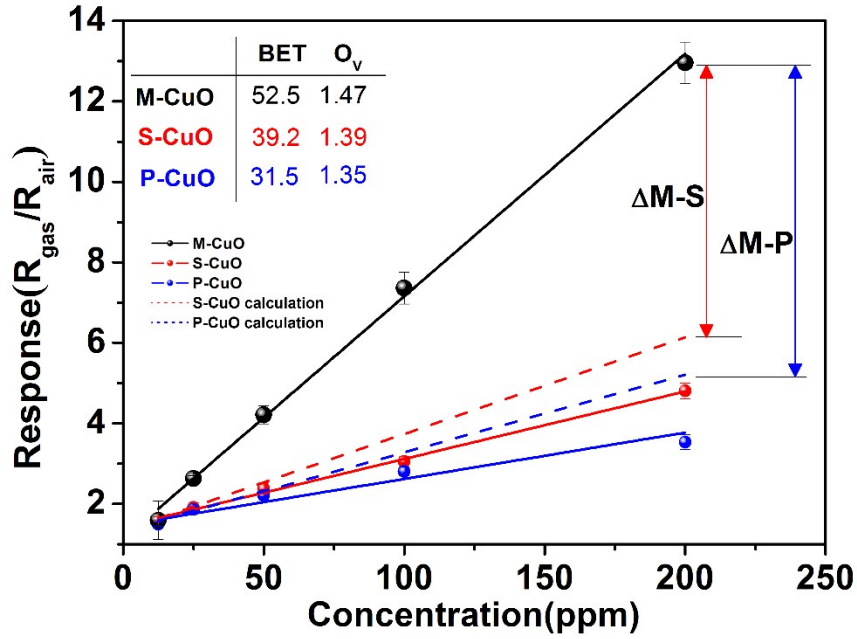


Fig. S16 Comparison of the experimental and calculated sensitivity as a function of ethanol concentration. The solid black, red and blue lines represent the experimental results of M-CuO, S-CuO and P-CuO, respectively, while the dashed red and blue lines indicate the calculation results of S-CuO and P-CuO, respectively, which were obtained by simply multiplying the experimental values of S-CuO or P-CuO with a H coefficient determined as below.

$$H_{M-S} = \frac{S_{M-CuO}}{S_{S-CuO}} \times \frac{O_{V M-CuO}}{O_{V S-CuO}} \approx 1.42 \quad (S1)$$

$$H_{M-P} = \frac{S_{M-CuO}}{S_{P-CuO}} \times \frac{O_{V M-CuO}}{O_{V P-CuO}} \approx 1.8 \quad (S2)$$

Where S_{M-CuO} , S_{S-CuO} , S_{P-CuO} are the surface areas of M-CuO, S-CuO and P-CuO, respectively, $O_{V M-CuO}$, $O_{V S-CuO}$ and $O_{V P-CuO}$ are the number of oxygen vacancies in M-CuO, S-CuO and P-CuO, respectively.

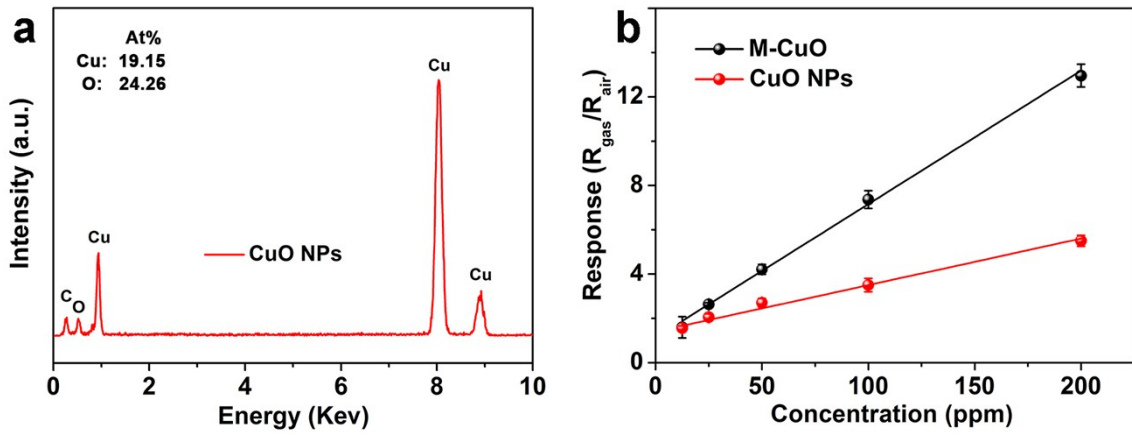


Fig. S17 Composition and gas sensing properties of the sensor containing CuO nanoparticles.

(a) EDS of CuO nanoparticles. (b) Response to ethanol at different concentrations with the M-CuO sensor as reference.

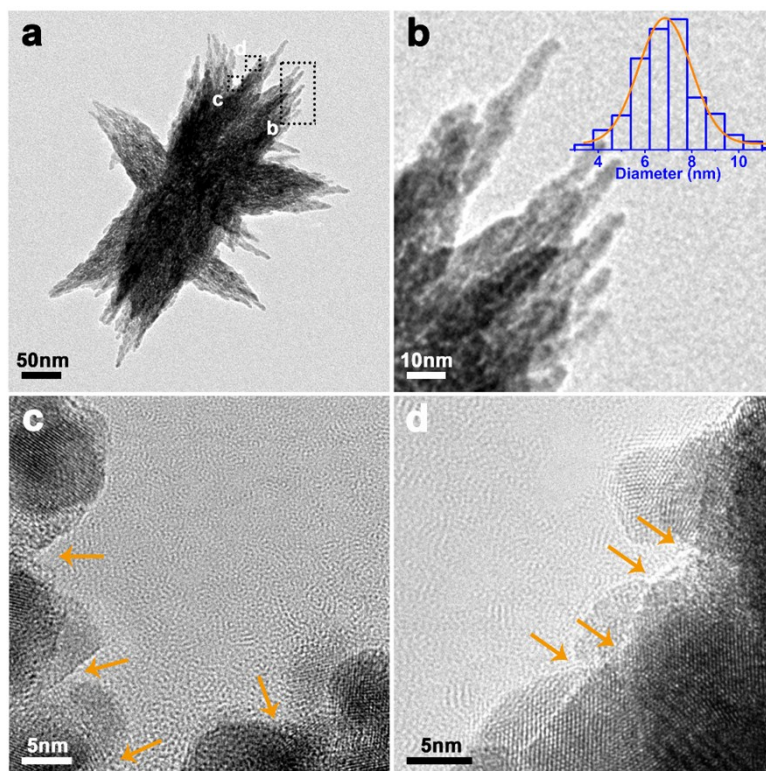


Fig. S18 Characterizations of necking sites of M-CuO. (a) TEM image of a M-CuO bundle. (b) Enlarged image of selected area b in (a), the average size of nanoparticles is 7nm (the inset). (c) and (d) HRTEM images of selected area c and d (a).

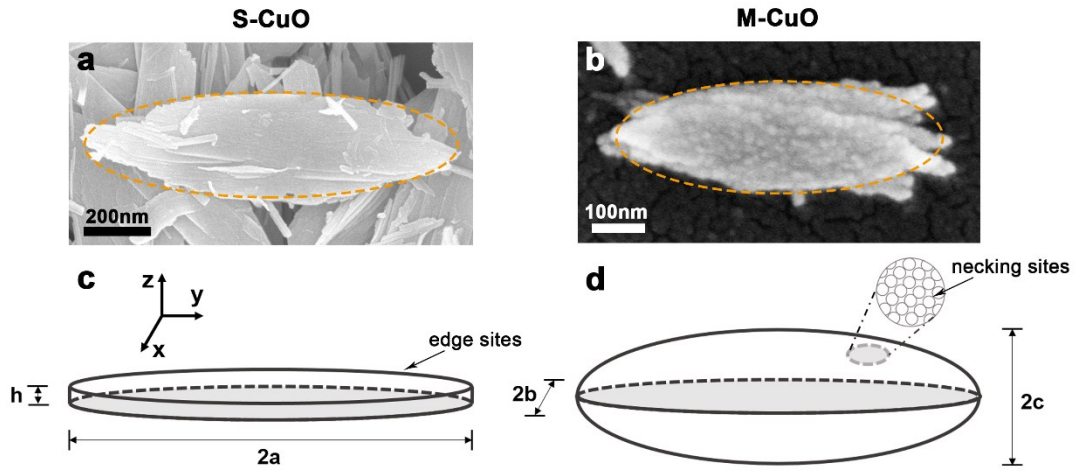


Fig. S19 Mathematical model for calculating the adsorption sites of S-CuO and M-CuO.

According to the SEM image in Fig. S19a, S-CuO exhibits a shape of elliptical sheet with a semi-major axis of $a=1000$ nm, semi-minor axis $b=150$ nm and height $h=90$ nm. The sheet edge was regarded as the adsorption sites. In contrast, M-CuO presents spindle-like morphology (see SEM image in Fig. 19b) which can be simplified as an ellipsoid with a semi-major axis $a = 300$ nm, semi-minor axis $b = 100$ nm and height $c = 100$ nm according to the statistics of SEM images, approximately. The radius (r) of component CuO nanoparticles is 4.5 nm. The total length of adsorption sites (TLAS) can be determined as the half of total perimeters of the nanoparticles on tangent plane of the M-CuO ellipsoid. We calculated the ratio of the specific surface area of M-CuO to that of S-CuO, the result, 1.35, is very close to the experimental value, 1.34 (see Fig. S13), which verifies the feasibility of the mathematical models. Further, the TLAS per surface area was calculated for M-CuO and S-CuO, and the value of M-CuO was determined as ten times of that of S-CuO.

(1) Basic mathematical formulas

The area of an ellipse: $S_{ee} = \pi ab$

The surface area of an ellipsoid: $S_{ed} = \frac{4}{3} \pi (ab + bc + ac)$

The area of a circle: $S_c = \pi r^2$

The surface area of a sphere: $S_s = 4\pi r^2$

The volume of an ellipsoid: $V_{ed} = \frac{4}{3} \pi abc$

The volume of a sphere: $V_s = \frac{4}{3}\pi r^3$

The perimeter of an ellipse: $L_{ee} = 2\pi b + 4(a - b)$

The perimeter of a circle: $L_c = 2\pi r$

(2) The number of particles on ellipsoid surface

$$N_{NPs} = \frac{S_{ed}}{S_c} = \frac{4(ab + bc + ac)}{3r^2} \quad (S3)$$

(3) The specific surface area of S-CuO

$$S_S = \frac{\sum S}{m} = \frac{2S_{ee} + L_{ee} \times h}{S_{ee} \times h \times \rho} = \frac{2\pi ab + [2\pi b + 4(a - b)] \times h}{\pi abh\rho} \quad (S4)$$

(4) The specific surface area of M-CuO

$$S_M = \frac{S}{\sum m} = \frac{N_{NPs} \times \frac{1}{2} S_c}{\left(V_{ed} + \frac{N_{NPs}}{2} \times V_s \right) \rho} = \frac{6(ab + bc + ac)}{[3abc + 2(ab + bc + ac)r] \rho} \quad (S5)$$

(5) The ratio of specific surface area between M-CuO and S-CuO

$$\frac{S_M}{S_S} \approx 1.35 \quad (S6)$$

(6) The overall edge length of S-CuO

$$L_S = 2L_{ee} = 4\pi b + 8(a - b) \quad (S7)$$

(7) The overall edge length of M-CuO

$$L_M = \frac{L_c \times N_{NPs}}{2} = \frac{4\pi(ab + bc + ac)}{3r} \quad (S8)$$

(8) The edge length of S-CuO per unit specific surface area

$$D_S = \frac{L_S}{S_S} \quad (S9)$$

(9) The edge length of M-CuO per unit specific surface area

$$D_M = \frac{L_M}{S_M} \quad (S10)$$

(10) The ratio of adsorption active sites length per specific surface area between M-CuO and S-CuO

$$\frac{D_M}{D_S} \approx 10 \quad (S11)$$

- 2 G. X. Zhu, H. Xu, Y. Y. Xiao, Y. J. Liu, A. H. Yuan, X. P. Shen, *ACS Appl. Mater. Interfaces*. 2012, **4**, 744-751.
- 3 C. Yang, X. T. Su, F. Xiao, J. K. Jian, J. D. Wang, *Sensors and Actuators B*. 2011, **158**, 299-303.
- 4 A. S. Zoolfakar, M. Z. Ahmad, R. A. Rani, J. Z. Ou, S. Balendhran, S. Zhuiykov, K. Latham, W. Wlodarski, K. Kalantar-zadeh, *Sensors and Actuators B*. 2013, **185**, 620-627.
- 5 S. H. Park, H. S. Ko, S. Y. An, W. I. Lee, S. M. Lee, C. M. Lee, *Ceramics International*. 2013, **39**, 5255-5262.
- 6 C. Yang, F. Xiao, J. D. Wang, X. T. Su, *J. Colloid Interface Sci*. 2014, **435**, 34-42.
- 7 J. J. Wu, Q. W. Huang, D. W. Zeng, S. P. Zhang, L. Yang, D. S. Xia, Z. D. Xiong, C. S. Xie, *Sensors and Actuators B*. 2014, **198**, 62-69.
- 8 D. A. Svintsitskiy, A. I. Stadnichenko, D. V. Demidov, S. V. Koscheev, A. I. Boronin, *Applied Surface Science*. 2011, **257**, 8542-8549.
- 9 D. A. Svintsitskiy, A. P. Chupakhin, E. M. Slavinskaya, O. A. Stonkus, A. I. Stadnichenko, S. V. Koscheev, A. I. Boronin, *J. Mol. Catal. A-Chem*. 2013, **368-369**, 95.
- 10 J. W. Zhao, C. S. Xie, L. Yang, S. P. Zhang, G. Z. Zhang, Z. M. Cai, *Applied Surface Science*. 2015, **330**, 126-133.
- 11 F. W. Jason, B. H. Car, *J. Phys. Chem*. 1994.